The Astronomical Journal, 137:3761–3777, 2009 April doi:10.1088/0004-6256/137/4/3761

ULTRAVIOLET QUASI-STELLAR OBJECTS

Luciana Bianchi[1], John B. Hutchings[2], Boryana Efremova[3], James E. Herald[3], Alessandro Bressan[4,5], and Cristopher Martin[6]

[1] Department of Physics and Astronomy, Johns Hopkins University, 3400 North Charles Street, Baltimore, MD 21218, USA; bianchi@pha.jhu.edu
[2] The National Research Council of Herzberg Institute of Astrophysics, Canada
[3] Center for Astrophysical Sciences, Johns Hopkins University, Baltimore, MD, USA
[4] INAF–Astronomical Observatory of Padova, Padova, Italy
[5] INAOE, Tonantzintla (Puebla), Mexico
[6] California Institute of Technology, Pasadena, CA, USA

Received 2008 May 20; accepted 2008 December 27; published 2009 March 4

ABSTRACT

We present a sample of spectroscopically confirmed quasi-stellar objects (QSOs) with FUV–NUV color (as measured by *Galaxy Evolution Explorer* (*GALEX*) photometry, FUV band: 1344–1786 Å, NUV band: 1771–2831 Å) bluer than canonical QSO templates and than the majority of known QSOs. We analyze their FUV to NIR colors, luminosities, and optical spectra. The sample includes a group of 150 objects at low redshift ($z < 0.5$), and a group of 21 objects with redshift $1.7 < z < 2.6$. For the low-redshift objects, the "blue" FUV–NUV color may be caused by enhanced Lyα emission, since Lyα transits the *GALEX* FUV band from $z = 0.1$ to $z = 0.47$. Synthetic QSO templates constructed with Lyα up to three times stronger than in standard templates match the observed UV colors of our low-redshift sample. Optical photometric and spectroscopic properties of these QSOs are not atypical. The Hα emission increases, and the optical spectra become bluer, with increasing absolute UV luminosity. The lack of selected objects at intermediate redshift is consistent with the fact that for $z = 0.48$–1.63, Lyα is included in the *GALEX* NUV band, making the observed FUV–NUV redder than the limit of our sample selection. The UV-blue QSOs at redshift ∼2, where the *GALEX* bands sample rest-frame ≈450–590 Å (FUV) and ≈590–940 Å (NUV), are fainter than the average of UV-normal QSOs at similar redshift in NUV, while they have comparable luminosities in other bands. Therefore, we speculate that their observed FUV–NUV color may be explained by a combination of steep flux rise toward short wavelengths and dust absorption below the Lyman limit, such as from small grains or crystalline carbon (nanodiamonds). The ratio of Lyα to C IV could be measured in 10 objects; it is higher (30% on average) than for UV-normal QSOs, and close to the value expected for shock or collisional ionization. However, optical spectra are taken at different times than the UV photometry, which may bias the comparison if lines are variable. These QSO groups are uniquely set apart by the *GALEX* photometry within larger samples, given that their optical properties are not unusual.

Key words: quasars: absorption lines – quasars: emission lines – quasars: general – ultraviolet: galaxies

Online-only material: color figures, machine-readable and VO tables

1. INTRODUCTION

In all quasi-stellar object (QSO) samples, there is concern that selection effects are present and significant, particularly in whether whole classes of objects are not included, or even known. This study aims at characterizing a population of objects with rising fluxes at UV-observed wavelengths. Following our work of classification of UV sources from the *GALEX*[7] sky surveys (Bianchi 2008; Bianchi et al. 2005, 2006, 2007, 2008; Hutchings & Bianchi 2008 and references therein), we have suspected the existence of a substantial number of extragalactic objects with FUV–NUV color much bluer (more negative) than canonical QSO templates and than the majority of QSOs in known samples. Such objects are rather "normal" at optical wavelengths (spectroscopically and photometrically) but they stand out in the observed UV range, having FUV–NUV colors similar to those of hot white dwarfs (WDs). Photometrically, these objects have UV-to-optical colors similar to a stellar binary containing a hot WD and a cooler companion. That a significant number of "FUV–NUV" blue extragalactic objects existed was first suspected by Bianchi et al. (2007), based on density counts of photometrically selected WD candidates. In fact, the number of objects per square degree whose spectral energy distribution (SED; FUV to NIR) is consistent with a single hot WD increases with magnitude down to $m_{\rm UV} \sim 21$ (AB) and then declines, consistent with Milky Way (MW) models. However, the density of objects with similarly blue UV color but redder optical colors, that we would expect to be hot WDs with a cool companion, increases considerably at fainter magnitudes, suggesting that a significant number of faint extragalactic objects may be included in the color–color *locus* of these stellar binaries (Bianchi et al. 2007; Bianchi 2008). In this work, we focus on these QSOs, which display very blue observed FUV–NUV colors, and investigate whether their properties are unlike those of known objects.

2. SAMPLE AND DATA

The sample was extracted from the catalog of matched UV/optical sources of Bianchi (2008), obtained by matching the

[7] The *Galaxy Evolution Explorer* (*GALEX*; Martin et al. 2005), is a NASA Small Explorer performing imaging surveys of the sky in two UV bands simultaneously: FUV (1344–1786 Å, $\lambda_{\rm eff} = 1538.6$ Å) and NUV (1771–2831 Å, $\lambda_{\rm eff} = 2315.7$ Å) with different coverage and depth. See Bianchi (2008) for a summary of the UV sources classification and statistics in the main surveys, and Morrissey et al. (2007) for instrument description and performance.

UV sources in the *GALEX* third data release (GR3),[8] to the Sloan Digital Sky Survey (SDSS) sixth data release (DR6). *GALEX* provides sky surveys with different sky area coverage and depth: we restricted this work to the "Medium Imaging Survey" (MIS) data, which reaches a typical AB mag of ≈22.7 in both FUV and NUV. The overlap area between *GALEX*-GR3 MIS data and SDSS-DR6 is 573 deg^2 (Bianchi 2008), taking into account that only the central 1° diameter part of the *GALEX* fields was used in our master catalog, to assure homogeneous photometry quality and exclude defects in the outer parts of the circular field. For each matched source, *GALEX* provides FUV (1344–1786 Å, $\lambda_{\rm eff}$ = 1538.6 Å) and NUV (1771–2831 Å, $\lambda_{\rm eff}$ = 2315.7 Å) photometry, and the SDSS provides u, g, r, i, z photometry. More details on the matchings procedure and the catalog are given by Bianchi (2008) and L. Bianchi et al. (2009, in preparation).

In order to characterize the suspected "FUV–NUV blue" QSOs, we extracted from the matched UV/optical source catalog of Bianchi (2008) the spectroscopically confirmed QSOs with FUV–NUV < 0.1 (AB mag): this FUV–NUV limit is "bluer" (more negative) than the synthetic FUV–NUV color from the two QSO canonical templates used by Bianchi et al. (2007), which represent average QSO properties, at any redshift. The colors of the canonical templates are shown in Figures 1 and 2 (cyan diamonds) as a function of redshift. We will refer to this sample as "UV-blue" QSOs for brevity throughout the paper. It is restricted to sources with photometric errors smaller than 0.3 mag in both FUV and NUV, and color FUV–NUV < 0.1, for which SDSS spectroscopy exists and gives a "QSO" classification. The requirement of available SDSS spectroscopy effectively limits the sample to brighter magnitudes, but it provides a classification and useful information, which will help interpreting larger samples of photometric candidates. Such relatively bright objects will also be accessible to the spectroscopic capabilities of the refurbished *Hubble Space Telescope* (*HST*), and to other follow-up observations. Note that the SDSS spectroscopic class "QSO" (class 4) probably also includes Seyfert galaxies. We will use here the generic term "QSO" to reflect our selection criterion from the SDSS spectroscopic database. It is important to note that spectroscopic targets in the SDSS were selected with criteria unrelated to our present objective and therefore our UV-blue spectroscopically confirmed QSOs may be a biased subsample among the UV-blue QSO photometric candidates.

These selection criteria produced an initial sample of 174 objects. One additional object was excluded because its u-band measurement is saturated. The photometric properties of the sample QSOs are presented in Section 3, and their optical spectra and overall properties are analyzed in Section 4. The selected objects are shown in two color–color diagrams, Figures 1 and 2, where they can be compared with other classes of objects, in particular hot stars, typical QSOs, and galaxies. Our analysis of the spectra (Section 4) generally confirms the redshift measurement from the pipeline. However, we found that one object (*GALEX* J172101.08+532433.7, R.A. = 260.2544916, decl. = 53.4093516, SDSS match id= 587725490527731868) was misclassified by the SDSS spectroscopic pipeline as a QSO with redshift z = 2.7: its spectrum is that of a hot star. It is shown in some figures because it is interesting to note its position in the color–color diagrams (Figures 1 and 2): the *GALEX* photometry clearly place this object on the stellar sequence and not as a QSO candidate. Coordinates, photometry, and other relevant information are given in Table 1, and sample images are shown in Figure 3.

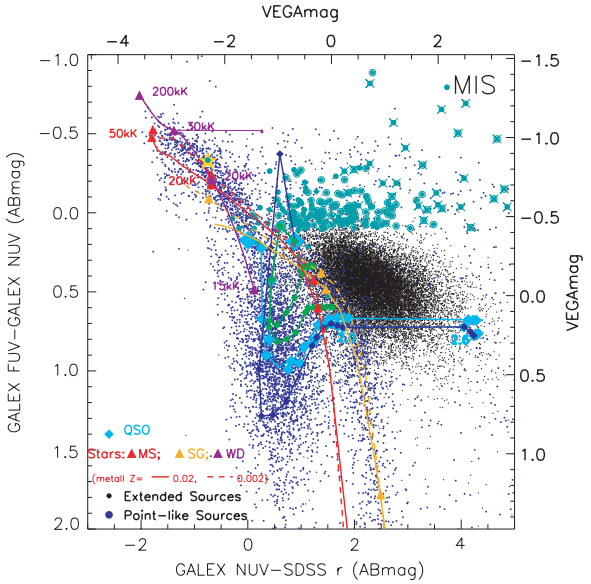

Figure 1. Color–color diagram showing the catalog of GR3-MIS UV sources of Bianchi (2008), with blue dots for pointlike sources and black dots for extended sources (essentially galaxies). Our UV-blue QSOs are shown with teal dots (circled for extended sources, and marked with an X when the FUV–NUV error is >0.15). Synthetic colors for QSO templates are shown with diamonds (cyan: standard templates, dark blue: templates with three times enhanced Lyα emission; dark green: templates with $F_\lambda \sim \lambda^{-0.6}$ and $F_\lambda \sim \lambda^{-1.2}$ in EUV. The redshift values marked by the diamonds are z = 0 (largest cyan diamonds, near the center), 0.2, 0.4, 0.6, 1.0, 1.2, 1.4, 1.6, 1.8, 2.0 (labeled), 2.2, 2.4, 2.6 (labeled), 3.0. Stellar sequences are shown (red, yellow, and purple triangles for $\log g$ = 3, 5, and 9), with $T_{\rm eff}$ values marked. A reddening arrow for $E(B-V) = 0.3$ is shown on a WD ($T_{\rm eff}$ = 30 kK) model point. The yellow star is the stellar object misclassified by the SDSS pipeline as a QSO. The majority of UV-normal QSO follows the template tracks, below and to the left of the stellar sequence.

The SDSS optical spectra (range ∼3800–9200 Å, resolution ∼1800) provide the initial classification as QSOs and a measure of redshift for the objects. Our sample includes a group of 151 objects at low redshift (0.041 < z < 0.436), and 21 objects with redshift between 1.7 and 2.6, all pointlike. Only one object has intermediate redshift (z = 0.93) and its identification as a QSO is dubious. It has fairly large photometric errors: FUV = 21.49 ± 0.12, NUV = 21.43 ± 0.10, but the typical QSO FUV–NUV color at this redshift is much redder (by >1 mag, see Figure 1); therefore, if it is a QSO it would be quite anomalous. At this redshift, the *GALEX* bands sample rest wavelengths of ∼1300 Å (NUV) and ∼800 Å(FUV), and a very blue FUV–NUV color would not be expected. The image and spectrum of this object are shown in Figure 4 (bottom). The spectrum shows one emission line that is identified as Mg II for the alleged redshift and possibly a few absorptions including one at the red end that could be Hγ. The observed wavelengths of the lines are not obvious for identification, assuming other values of redshift the observed line(s) might be [C III] λ1909 or [O II] λ3727, but then other lines such as [C IV] λ1550 or [O III] λ5007 should be present and are not. So, either z = 0.93 is right or perhaps the emission is some artifact in the spectrum. Therefore, we consider this object doubtful and do not include it in our analysis. The lack of objects between redshift 0.5 and 1.7 is consistent with our selection of very blue FUV–NUV color, because Lyα is in the NUV band between z = 0.48 and z = 1.63, causing brighter

[8] GR3 is available from the MAST archive at http://galex.stsci.edu.

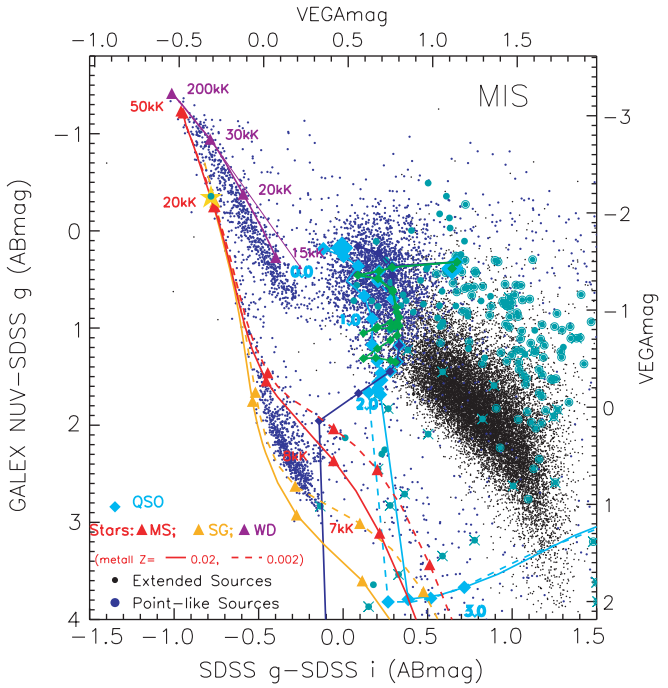

Figure 2. Color–color diagram including the $g-i$ color. Symbols as in previous figure. In this plot, the NUV–g color separates the high- and low-redshift QSOs (redshift values marked in cyan along the template, $z = 0$ is the large diamond at the top of the sequence. The cluster of pointlike sources close to the low-z QSO template colors are normal QSOs. The extended sources among our UV-blue QSOs have $g-i$ redder than QSOs templates, and in the $g-i$ color range of galaxies, reflecting the contribution from the underlying galaxy, but they are bluer than the galaxies in NUV–g. This diagram further separates the single hot stars from the UV-blue QSOs (note again the location of the spectroscopically misclassified object, plotted as a yellow star).

flux in NUV and consequently much redder FUV–NUV color, as can be seen in Figure 1.

We also caution that while the *GALEX* FUV and NUV images are taken simultaneously, the SDSS imaging was taken at a different time from the *GALEX* observations, therefore any significant variability may affect the combined UV and optical colors, such as NUV–r. For this reason, we based our initial sample selection on the FUV–NUV color only. Some of our targets have repeated observations with *GALEX*, but most repeated measurements are from the All-sky Imaging Survey (AIS), which has about 10 times shorter exposures than MIS (used in this work) and therefore large photometric uncertainties. In a few cases, repeated measurements are discrepant by $>2\sigma$ in the combined photometric errors: however, most of the discrepant measurements have artifact flags set. We compile for completeness all repeated measurements with exposures longer than 400 s and formally discrepant by $>2\sigma$ in Table 2, where we also provide comments that help assess reliability, based on the flags from the pipeline photometry, and our visual inspection of the images. We only excluded measurements on the very edge of the *GALEX* field (flag "rim"), however we did not apply error cuts nor area cut, for the purpose of an exhaustive comparison, while our analysis sample is restricted to measurements in the central $0.^{\circ}5$ radius of the field for accurate photometry (Section 2). In a few cases, the discrepancies in the repeated measurements cannot be ascribed to artifacts, and these objects may deserve dedicated follow-up photometry. In some cases the variation affects the FUV–NUV color, and in particular some repeated measurements have redder FUV–NUV than our initially selected data set. All discrepant repeated measurements with MIS exposures (two high-redshift objects and 10 low-redshift objects) have FUV–NUV >0.1. If we also consider AIS data (exposure times $\sim$100 s), we find 55 additional repeated measurements discrepant by $>2\sigma$, of which 36 give FUV–NUV redder than our selected data set (MIS measurements), and other 19 bluer. Fast variability is not unknown in QSOs, and in particular line strength may vary on short timescales, while it would be less plausible for dust effects to change rapidly. We stress that a variability assessment however would require custom photometry, and while the standard pipeline photometry is good for statistical analysis, such as the scope of this work, we should refrain from overinterpreting individual measurements and individual variations. Other 72 AIS and seven MIS repeated measurements agree within 2σ with our selected measurements given in Table 1. One object in the initial sample, although part of the MIS survey, has a 40 s exposure in FUV and 1518 s in NUV: although its FUV error (0.23) meets our selection limits, a longer MIS exposure of 853 s in both FUV and NUV and smaller errors gives FUV–NUV $= 0.17$, so it is eliminated from our analysis sample.

A larger sample of about 30,000 QSO candidates with "normal" FUV–NUV colors (i.e., similar to the standard template), extracted from the matched UV/optical source catalog of Bianchi (2008) will be presented elsewhere. We will refer to this sample as "UV-normal" in the discussion of the UV-blue sample for comparison purposes.

3. GENERAL PHOTOMETRIC PROPERTIES

Of the 174 sample objects, 64 sources are classified as pointlike (at the resolution of the SDSS imaging, $\sim 1.''4$) and 110 as extended (all at low redshift), by the SDSS pipeline. We will keep the pipeline classification because it is derived from an objective procedure, although the result depends on the contrast between central source and underlying galaxy. *GALEX* and SDSS imaging for a subsample of objects, presented in Figure 3, shows that the definition of "pointlike" (P) or "extended" (E) is not clear-cut.

The sample selection, as described in Section 1, was restricted to MIS sources with photometric errors less than 0.3 mag in FUV and NUV. Of the 64 pointlike sources, 42/33 have errors less than 0.1 mag/0.05 mag, and only four have errors between 0.2 and 0.3 mag, in FUV. As for the NUV measurements, 36/45 pointlike sources have errors $<0.05/0.1$ mag, and 10 have errors larger than 0.2 mag. In the r band, all but two objects have errors smaller than 0.05 mag (one object has an error of 0.14 mag, and one of 0.08 mag). Of the 110 extended objects, 108 have r-band error <0.04 mag, 97/94 have NUV/FUV error <0.1 mag. Sources with large photometric errors are identified in the figures. Most objects with larger errors are in the $z \sim 2$ group. At this redshift, our color cut of FUV–NUV <0.1 is more than half a magnitude bluer than the average value for UV-normal QSOs (e.g., Figure 1), therefore these objects may be truly extreme with respect to average samples in spite of their large photometric errors. We point out that the object *GALEX* J113223.4+641958 (SDSS J113223.42+641958.4) has a u-band magnitude of 28.7 ± 0.46 (petromag), while the magnitude listed on the explorer page for this object is $u = 25.07 \pm 3.05$. It has no artifact flags, the pipeline records only a warning: "no petrosian radius could be determined. Petrosian magnitude still usable; the object is blended with an extended object." The surrounding galaxy can be seen in the SDSS imaging with a radius of about $5''$. We regard

Table 1
The UV-Blue QSO Sample

GALEX IAU ID	R.A. (deg)	Decl. (deg)	FUV (AB)	NUV (AB)	u (AB)	g (AB)	r (AB)	i (AB)	z (AB)	Redshift	$E(B-V)$	Comment
High-Redshift QSOs ($z > 1$)												
GALEX J075627.72+205415.1	119.1154984	20.9041836	21.00 ± 0.15	21.82 ± 0.14	20.23 ± 0.09	19.72 ± 0.02	19.52 ± 0.03	19.22 ± 0.04	19.22 ± 0.15	2.21	0.06	Pointlike
GALEX J025221.08−085516.0	43.0878540	−8.9211193	20.88 ± 0.09	21.67 ± 0.11	18.56 ± 0.03	18.03 ± 0.01	17.94 ± 0.01	17.85 ± 0.02	17.50 ± 0.04	2.29	0.05	Pointlike
GALEX J161821.57+492603.0	244.5898736	49.4341532	22.05 ± 0.18	22.74 ± 0.23	19.23 ± 0.04	18.64 ± 0.01	18.66 ± 0.01	18.63 ± 0.02	18.38 ± 0.05	2.28	0.02	Pointlike
GALEX J222323.21−084740.5	335.8467089	−8.7945764	22.35 ± 0.14	23.01 ± 0.25	19.52 ± 0.05	19.47 ± 0.02	19.38 ± 0.02	19.14 ± 0.03	19.00 ± 0.10	1.99	0.05	Pointlike
GALEX J145645.30+595436.2	224.1887297	59.9100553	22.57 ± 0.19	23.14 ± 0.29	20.52 ± 0.08	20.31 ± 0.03	20.41 ± 0.04	20.44 ± 0.07	19.97 ± 0.15	2.17	0.01	Pointlike
GALEX J211858.56−063027.3	319.7439988	−6.5075842	22.17 ± 0.17	22.58 ± 0.19	19.97 ± 0.06	19.75 ± 0.02	19.62 ± 0.02	19.48 ± 0.04	19.27 ± 0.11	2.00	0.11	Pointlike
GALEX J082337.98+455621.4	125.9082468	45.9392840	22.41 ± 0.19	22.67 ± 0.29	22.22 ± 0.80	21.40 ± 0.23	20.86 ± 0.14	20.33 ± 0.09	19.46 ± 0.11	2.59	0.04	Pointlike
GALEX J003505.58−103536.4	8.7732425	−10.5934493	22.46 ± 0.23	22.68 ± 0.25	19.35 ± 0.04	18.57 ± 0.01	18.62 ± 0.01	18.49 ± 0.01	18.20 ± 0.05	2.26	0.03	Pointlike
GALEX J230724.98+000958.0	346.8540794	0.1661096	21.93 ± 0.15	22.12 ± 0.10	19.40 ± 0.06	19.41 ± 0.02	19.33 ± 0.03	19.04 ± 0.03	19.23 ± 0.17	1.90	0.04	Pointlike
GALEX J113638.68+011031.5	174.1611550	1.1754105	21.94 ± 0.18	22.13 ± 0.20	19.83 ± 0.05	19.68 ± 0.02	19.60 ± 0.03	19.47 ± 0.04	19.17 ± 0.11	2.13	0.02	Pointlike
GALEX J155013.52+033744.6	237.5563540	3.6290531	22.74 ± 0.25	22.86 ± 0.27	19.54 ± 0.05	19.51 ± 0.02	19.33 ± 0.02	18.93 ± 0.03	18.76 ± 0.09	1.91	0.10	Pointlike
GALEX J233139.76+010428.7	352.9156781	1.0746313	20.56 ± 0.07	20.67 ± 0.07	18.93 ± 0.03	18.54 ± 0.01	18.45 ± 0.01	18.53 ± 0.01	18.40 ± 0.05	2.25	0.04	Pointlike
GALEX J090814.51+550701.6	137.0604696	55.1171069	22.98 ± 0.17	23.03 ± 0.22	20.21 ± 0.06	19.84 ± 0.02	19.46 ± 0.02	19.07 ± 0.02	18.90 ± 0.08	1.93	0.02	Pointlike
GALEX J015229.22−083640.0	28.1217418	−8.6111176	22.43 ± 0.19	22.47 ± 0.19	20.27 ± 0.10	19.84 ± 0.03	19.27 ± 0.03	18.84 ± 0.03	18.83 ± 0.11	1.72	0.02	Pointlike
GALEX J020419.29+143929.2	31.0803956	14.6581219	21.07 ± 0.11	21.11 ± 0.09	19.11 ± 0.03	18.85 ± 0.01	18.80 ± 0.01	18.61 ± 0.02	18.43 ± 0.06	2.17	0.05	Pointlike
GALEX J082616.05+502049.5	126.5668879	50.3470827	22.58 ± 0.20	22.61 ± 0.27	19.19 ± 0.04	18.75 ± 0.01	18.62 ± 0.01	18.60 ± 0.02	18.37 ± 0.05	2.19	0.04	Pointlike
GALEX J005408.42−094637.1	13.5350664	−9.7769584	22.64 ± 0.28	22.68 ± 0.24	18.45 ± 0.02	18.06 ± 0.01	17.82 ± 0.01	17.61 ± 0.01	17.41 ± 0.03	2.13	0.04	Pointlike
GALEX J145055.62+015419.0	222.7317516	1.9052814	21.48 ± 0.12	21.45 ± 0.12	19.86 ± 0.05	19.77 ± 0.02	19.75 ± 0.03	19.56 ± 0.04	19.63 ± 0.18	1.87	0.04	Pointlike
GALEX J141807.07+050431.3	214.5294395	5.0753685	20.92 ± 0.09	20.87 ± 0.06	19.93 ± 0.06	19.56 ± 0.02	19.10 ± 0.02	18.72 ± 0.02	18.46 ± 0.05	1.89	0.03	Pointlike
GALEX J085344.92+565337.9	133.4371727	56.8938634	21.71 ± 0.13	21.63 ± 0.11	20.42 ± 0.14	20.45 ± 0.05	20.40 ± 0.08	20.12 ± 0.10	21.35 ± 1.50	1.86	0.05	Pointlike
GALEX J084658.13+465011.4	131.7422222	46.8364994	21.75 ± 0.08	21.66 ± 0.08	19.47 ± 0.04	19.36 ± 0.02	19.24 ± 0.02	19.14 ± 0.03	18.88 ± 0.07	2.12	0.02	Pointlike
Low-Redshift QSOs ($z < 1$)												
GALEX J075304.64+252436.6	118.2693129	25.4101641	19.78 ± 0.08	20.67 ± 0.06	19.36 ± 0.07	18.84 ± 0.02	18.33 ± 0.02	17.94 ± 0.02	17.72 ± 0.06	0.15	0.09	Extended
GALEX J154912.35+030641.8	237.3014425	3.1116111	22.45 ± 0.28	22.95 ± 0.28	21.62 ± 0.57	20.34 ± 0.06	19.01 ± 0.03	18.48 ± 0.03	17.96 ± 0.09	0.25	0.13	Extended
GALEX J140816.07+015528.5	212.0669475	1.9245728	22.26 ± 0.18	22.73 ± 0.29	20.50 ± 0.28	19.11 ± 0.03	18.06 ± 0.02	17.61 ± 0.02	17.23 ± 0.05	0.17	0.03	Extended

(This table is available in its entirety in machine-readable and Virtual Observatory (VO) forms in the online journal. A portion is shown here for guidance regarding its form and content.)

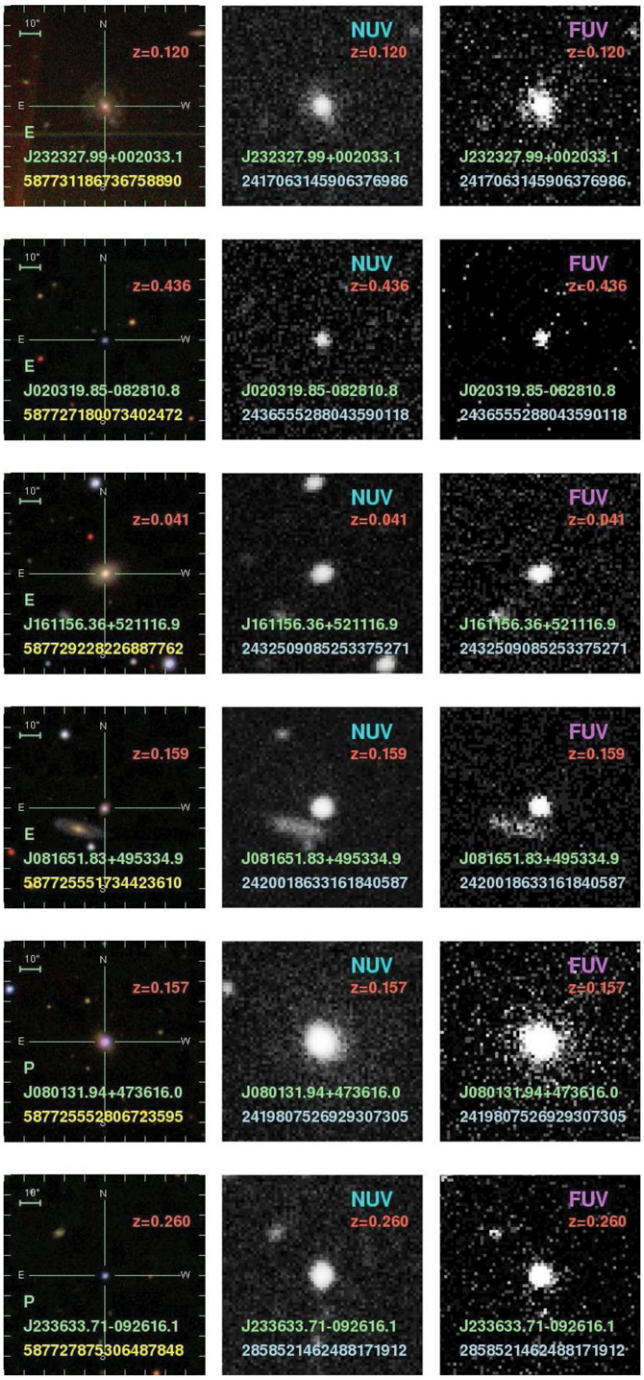

Figure 3. Sample imaging of our UV-blue QSOs. Each row shows one object. Columns left to right—first: color-composite SDSS image (resolution $\approx 1\farcs4$); second and third: *GALEX* NUV and FUV image, respectively (resolution $4\farcs2$ FUV/$5\farcs3$ NUV). The top four sources are classified as extended by the SDSS pipeline, the lower two objects as pointlike.

the petrosian magnitude as unreliable in the u band. Magnitudes in other bands for this object have smaller errors and seem more consistent among measurements. All other objects have u-band magnitudes brighter than 22.2, consistent with the SDSS limit (see Figure 3 of Bianchi et al. 2007). We give in Table 1 petrosian magnitude measurements for the SDSS data, for consistency among the sample and with other extragalactic works. The SDSS pipeline also provides magnitudes measured in different ways: psf fitting, de Vaucouleurs model, and exponential fitting. A description of the different magnitudes can be found on the SDSS Web site http://www.sdss.org/dr5/algorithms/photometry.html.

We checked for all objects whether the different measurements are discrepant. As expected, for pointlike sources the average difference is within the 1σ errors and the largest discrepancies close to 3σ. Disagreement between psf-mag and petromag tends to increase at longer wavelengths, where the extended galaxy is contributing. For extended objects, the measurements from petrosian and de Vaucouleur profile fitting agree on average within better than 2σ, while psf magnitudes are more discrepant as expected and should not be used.

The FUV–NUV and NUV–g colors of the sample objects are plotted as a function of redshift in Figure 5, and the FUV, NUV, and r-band magnitudes in Figure 6. "Extended" sources are plotted with different symbols, to explore possible trends, although the classification must be regarded only as an indication as pointed out above. Photometric errors (1σ error bars are shown) in most cases are quite small compared with the spread in FUV–NUV color observed in our sample. Figure 5 shows that the high-redshift objects have a wider range of FUV–NUV color than the low-redshift pointlike sample, although the spread may simply be caused by the large errors of these faint objects. The lack of extended objects at high redshift is likely due to the fact that for these more distant objects the same imaging does not reveal the underlying galaxy. This question will be investigated with deeper imaging aimed at revealing the underlying galaxy in the distant objects and to probe the contrast to the central source (Hutchings et al. 2009).

Figure 6 shows that low-redshift pointlike QSOs tend to be brighter than extended ones, in both FUV and NUV. In the r band, however, the magnitude spread is less (about 4 mag across the sample) and no preferential distribution is seen between pointlike and extended samples. Low-redshift pointlike objects are also brighter (observed magnitudes) than higher redshift objects by about 2–3 mag, but their intrinsic luminosity is lower. The distribution of observed magnitudes (left panels) is useful for comparison with other samples, and to estimate the possible contamination by these objects to density counts of other UV-blue objects such as MW WDs, which have similar FUV–NUV colors (see Bianchi et al. 2007, 2008, and Figure 1), as well as for planning follow-up observations. The misclassified star is shown in these panels. In the right-side panels of Figure 6, the absolute magnitudes are plotted (the luminosity distance was derived from the redshift using standard cosmology $H_0 = 70$ km s^{-1} Mpc^{-1}, $\Omega_M = 0.3$, $\Lambda = 0.7$); the distant objects are intrinsically more luminous. We plotted for comparison the median absolute magnitudes of our UV-normal QSO comparison sample (solid line in the right-side plots). The high-redshift UV-blue QSOs have luminosities similar to UV-normal QSOs, except in NUV, where they are fainter. The comparison suggests some absorption in the NUV band (rest-frame <900 Å for $z = 2$) as an explanation of their FUV–NUV color. We will discuss this point later.

4. ANALYSIS AND DISCUSSION

We discuss the two groups, $z < 0.5$, and $z \sim 2$ QSOs, separately because the FUV and NUV bands sample different rest-frame spectral regions and therefore the explanations for their blue FUV–NUV colors are different.

4.1. The Low-Redshift QSOs

The majority of our analysis sample has redshift <0.5 (150 objects, 109 extended, and 41 pointlike). Lyα transits the *GALEX* FUV band from $z = 0.1$ to $z = 0.47$, and this fact

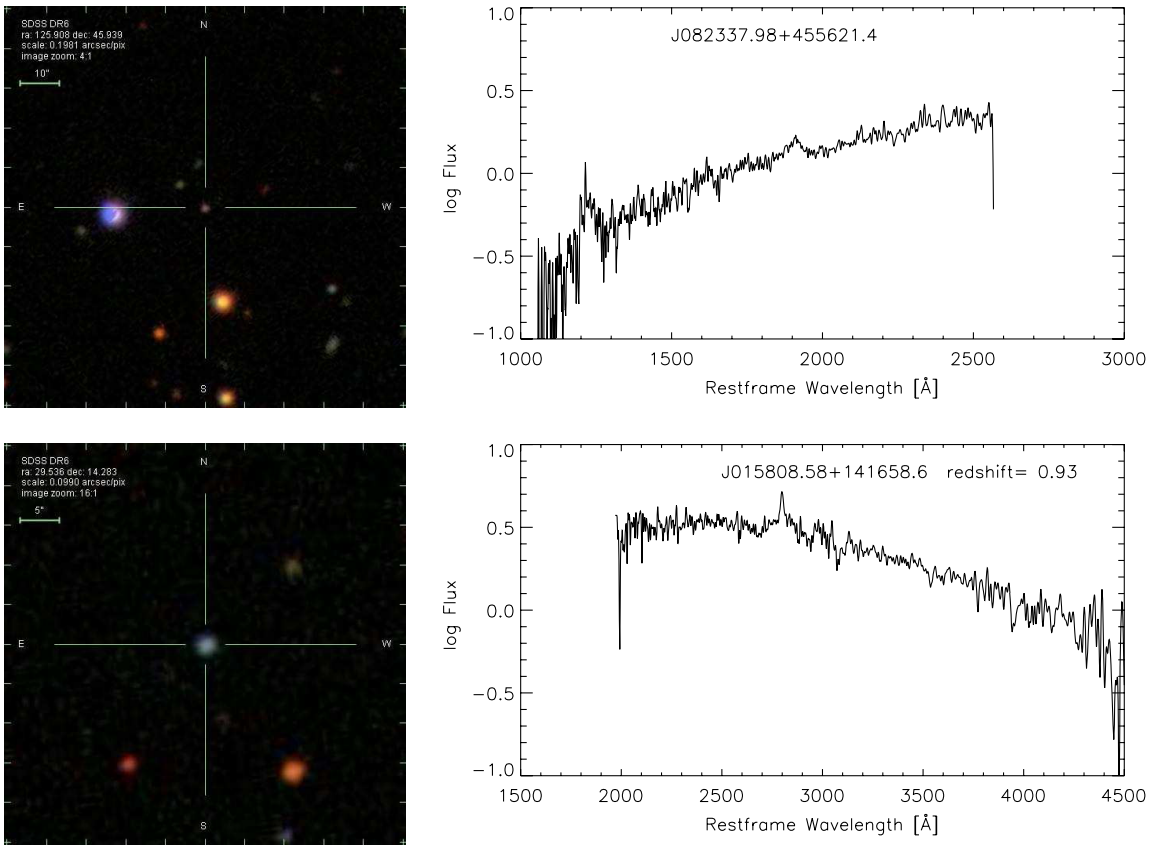

Figure 4. Two puzzling objects in the sample. Top: a "UV-blue" QSO with a red spectrum. The blue star nearby is further away than the match radius used of 4″. Bottom: the only object in the sample with redshift near to 1; its classification as a QSO is doubtful.

suggests that an intense Lyα emission may be the cause for the "FUV excess" of these objects. To test this hypothesis, we constructed templates with Lyα emission enhanced relative to standard templates, and derived their synthetic broadband colors. Such ad hoc templates with Lyα enhanced by up to three times match the range of observed FUV–NUV colors of our low-z sample, and are shown in Figures 1 and 2 (dark blue diamonds) together with synthetic colors from canonical templates (cyan diamonds), as well as in Figure 5 (top). Note from these figures that our simple cut of FUV–NUV <0.1 produced a low-redshift sample bluer in FUV–NUV than standard templates with a spread of about half a magnitude: the redder objects among our sample are very close to the standard template at $z \sim 0.2$, the UV-bluest objects differ by up to 0.5 mag (one by $\sim$1 mag) and are concentrated around $z \sim 0.2$ where Lyα is at the peak of the FUV filter transmission. The modulation with redshift of the hypothetical enhanced-Lyα effect, due to the filter transmission, is seen in the ad hoc template plotted in Figure 5.

None of our sample objects have UV spectra, which would directly reveal the cause of their blue FUV–NUV color. We examined their optical spectra and in particular Hα, the strongest line in all the objects. Figure 7 shows the optical spectra of our low-redshift sample, stacked, and compared with the standard template (cyan). The majority of the pointlike sources have emission lines stronger than the average template, and bluer spectral slope (flux increasing at shorter wavelengths). For the extended sources, however, line strength is generally typical and the spectral slope mostly redder than the standard template, reflecting the non-negligible contribution by the underlying galaxy (SDSS spectra are taken through a 3″ diameter aperture). Sample spectra for both pointlike and extended QSOs are also shown in Figure 8. There is a wide range of line strengths and profiles, as well as spectral slopes.

The SDSS pipeline provides automated measurements of width and equivalent width (EW) of the major lines, performed with line fitting; we downloaded and examined those quantities. We found that the centering of the line could be used, while line width and EW from the pipeline are not reliable for most spectra (examples in Figure 9). We remeasured the Hα line, first by hand to assess the difference from the pipeline measurements, and then with an ad hoc algorithm for more objective results. The line width estimated by our code is also shown in Figure 9. In order to minimize the complication of narrow absorptions and emissions in some profiles, we did not measure the width at half-maximum (peak) but the width at the average flux value of the total line emission. We consider our measurements more homogeneous than the pipeline values, as shown in Figure 9, and we use them in the following analysis. Hα width, EW, and fluxes (F_λ) measured (at rest-frame wavelengths) for the low-z sample are reported in Table 3. Errors from the spectra signal-to-noise ratio and continuum placement uncertainties, are estimated to be less than 10%. As a further check, measurements from our code agree with our manual measurements with by-eye location of the continuum to a few percent in all but a few cases, where they agree within 10%. Our measurements include the entirety of the emission feature, no attempt was made to separate narrow components when present, and no correction for [N II] was applied.

We searched for possible correlations of Hα intensity and width, and of the optical spectral slope, with the UV color and

Table 2
Objects with Repeated *GALEX* Observations Discrepant by $>2\sigma$ Error

GALEX IAU ID	FUV (AB)	NUV (AB)	Date (dd/mm/yy)	Exp. Time (s)	Matched *GALEX* ID	Dist ($''$)	FUV (AB)	NUV (AB)	Date (dd/mm/yy)	Exp. Time (s)	Survey	Comments
High-Redshift QSOs ($z > 1$)												
J230724.98+000958.0	21.93 ± 0.15	22.12 ± 0.10	9/9/2004	1697/3055	J230724.98+000958.4	0.44	21.61 ± 0.10	21.45 ± 0.08	8/24/2003	3181/3181	MIS	!
J005408.42-094637.1	22.64 ± 0.28	22.68 ± 0.24	9/23/2003	1666/1666	J005408.44-094637.7	0.71	23.14 ± 0.38	21.90 ± 0.14	9/25/2004	1648/1648	GII	
J085344.92+565337.9	21.71 ± 0.13	21.63 ± 0.11	1/17/2004	1694/1694	J085344.84+565338.6	1.00	22.05 ± 0.10	21.60 ± 0.09	1/17/2004	2959/2959	MIS	e E
Low-Redshift QSOs ($z < 1$)												
J075304.64+252436.6	19.79 ± 0.08	20.67 ± 0.06	2/14/2006	1703/1703	J075304.67+252436.6	0.53	...	20.45 ± 0.06	2/15/2006	1698/1698	MIS	epb E
J153219.90+033811.1	20.92 ± 0.13	21.20 ± 0.12	6/7/2003	828/828	J153219.90+033812.3	1.21	21.45 ± 0.19	20.91 ± 0.13	6/7/2003	476/476	MIS	
J223553.88+142805.7	19.78 ± 0.04	19.97 ± 0.03	8/13/2005	1608/3007	J223553.87+142806.0	0.35	19.76 ± 0.01	19.64 ± 0.01	8/23/2003	31533/31533	DIS	! EB
J160655.42+534016.9	18.98 ± 0.02	19.11 ± 0.02	6/25/2004	2862/2862	J160655.40+534016.7	0.29	19.71 ± 0.22	19.42 ± 0.01	5/2/2005	42/13341	DIS	! b B
J085318.52+551525.3	21.88 ± 0.14	21.98 ± 0.14	1/18/2004	1694/1694	J085318.57+551525.3	0.48	22.43 ± 0.19	22.06 ± 0.14	1/3/2006	1700/1700	GII	
J014248.83+142126.9	21.69 ± 0.14	21.78 ± 0.16	10/4/2004	1630/1630	J014248.85+142126.1	0.86	22.24 ± 0.16	21.94 ± 0.11	11/10/2004	1702/3391	GII	
J040446.72−045429.7	21.18 ± 0.10	21.24 ± 0.09	11/3/2004	2462/2462	J040446.73−045431.3	1.60	21.17 ± 0.12	20.58 ± 0.11	11/3/2004	1535/1535	MIS	! eb EPB
J013928.93−103425.9	20.81 ± 0.08	20.85 ± 0.06	10/15/2003	1579/1579	J013928.89−103426.5	0.77	20.59 ± 0.05	20.58 ± 0.04	12/13/2004	3284/3753	GII	!
J234019.81+005907.9	19.18 ± 0.02	19.20 ± 0.02	8/23/2003	3145/3145	J234019.83+005910.3	2.46	19.45 ± 0.04	19.19 ± 0.03	9/22/2006	1669/1669	MIS	! EP
J163142.50+465243.3	19.79 ± 0.04	19.76 ± 0.03	7/31/2004	2481/2481	J163142.54+465243.6	0.53	19.82 ± 0.04	19.68 ± 0.02	8/7/2004	2825/2825	MIS	e E
J235457.10+004220.5	18.25 ± 0.03	18.22 ± 0.02	10/22/2006	1108/1108	J235457.15+004220.3	0.72	18.34 ± 0.03	18.20 ± 0.02	10/21/2006	924/924	MIS	EB
J160545.93+532209.9	18.26 ± 0.02	18.22 ± 0.01	7/31/2004	1637/1637	J160545.98+532210.8	1.00	18.08 ± 0.12	17.86 ± 0.00	5/2/2005	42/13341	DIS	! PB
J032225.43−081255.3	18.93 ± 0.03	18.88 ± 0.02	11/29/2003	1698/1698	J032225.37−081255.4	0.90	18.92 ± 0.04	18.72 ± 0.02	11/30/2003	1698/1698	MIS	! e E
J160815.26+524450.8	19.46 ± 0.04	19.39 ± 0.03	7/31/2004	1635/1635	J160815.21+524451.3	0.71	19.86 ± 0.28	19.73 ± 0.01	5/3/2005	40/14866	DIS	! e EPB
J161156.36+521116.9	19.17 ± 0.04	19.09 ± 0.02	7/31/2004	1635/1635	J161156.35+521117.2	0.36	19.10 ± 0.04	19.00 ± 0.02	7/31/2004	1631/1631	NGS	! eb B
J005057.44+143753.7	21.34 ± 0.11	21.26 ± 0.10	9/25/2003	1687/1687	J005057.45+143753.8	0.21	21.70 ± 0.11	21.40 ± 0.09	8/30/2003	1967/1967	MIS	
J005328.80−085754.8	18.44 ± 0.02	18.36 ± 0.01	9/16/2003	1602/1602	J005328.79−085754.1	0.70	18.33 ± 0.02	18.22 ± 0.01	9/23/2003	1666/1666	MIS	!
J163625.47+421346.1	18.44 ± 0.02	18.35 ± 0.02	5/23/2004	1702/1702	J163625.48+421346.8	0.72	18.31 ± 0.03	18.26 ± 0.01	7/8/2004	1195/1586	DIS	!
...	...	...	...	...	J163625.42+421346.8	0.85	...	18.48 ± 0.00	5/5/2005	0/14689	DIS	! EPB
J233633.71−092616.1	18.44 ± 0.02	18.34 ± 0.01	9/2/2006	2189/2189	J233633.72−092616.9	0.82	18.42 ± 0.02	18.24 ± 0.01	9/27/2005	1973/2859	MIS	! eb EB

Notes. Explanation of comments: "!" denotes magnitude discrepancy (NUV or FUV) greater than 3σ, "E" denotes that the EDGE artifact flag is set, "P" denotes SExtractor flag 1 set (object has neighbors) "B" denotes SExtractor flag 2 set (object was originally blended with another one). Lower case flag codes for original sources, upper case for matched measurements.

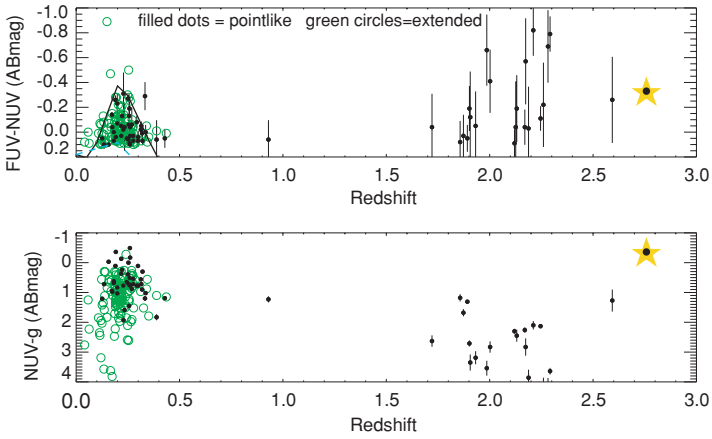

Figure 5. Measured FUV–NUV color and NUV–g color vs. redshift in the sample of UV-blue QSOs. Black dots indicate pointlike sources (at the SDSS resolution), and green/gray circles extended objects. The line in the top plot, visible for redshift ∼0.1–0.4, is the template with three times enhanced Lyα. The standard templates have redder colors, below the plot range. Observed colors are not dereddened. Applying reddening corrections (assuming foreground MW dust with $R_V = 3.1$) makes the FUV–NUV color more negative but insignificantly (dots would be higher by an amount about the size of the symbol at most) and decrease the NUV–g color by up to 0.2 mag. The yellow/gray star marks the source reclassified by us as a hot star, for the object at redshift $z = 0.93$; see the text. The lack of objects in the redshift range 0.5–1.7 is consistent with Lyα being in the NUV band in this range (Figure 1). The object at redshift $z = 2.6$ has a very red optical spectrum (Figure 4).

(A color version of this figure is available in the online journal.)

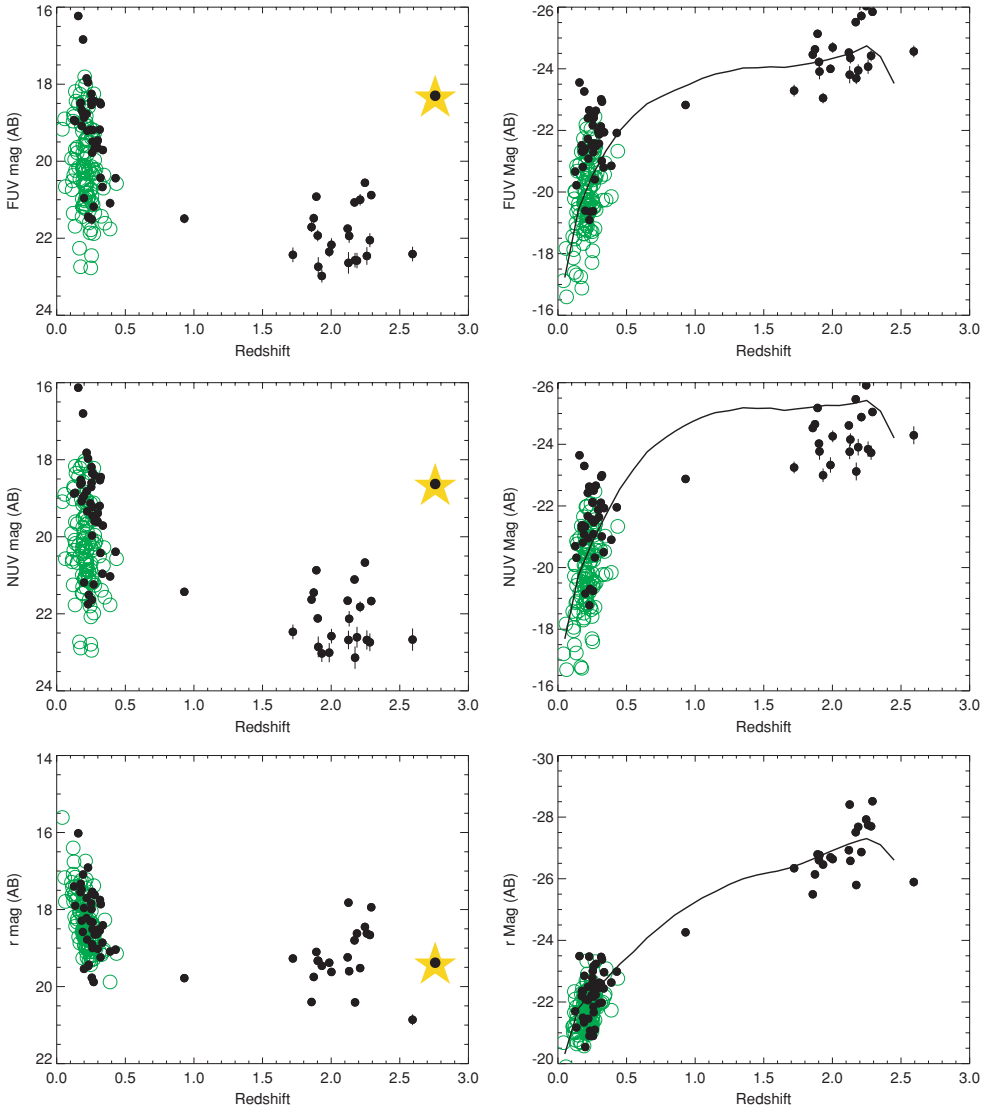

Figure 6. Left panels: FUV, NUV, and r-band magnitudes (observed, not dereddened) vs. redshift. Black dots are pointlike sources, green/gray circles are extended objects. Among the low-redshift QSOs, pointlike objects tend to be brighter than extended ones in both FUV and NUV, while they are similarly spread in the r-band magnitude. Right panels: absolute magnitudes, dereddened for foreground MW extinction. The solid line is the mean values of the UV-normal QSOs.

(A color version of this figure is available in the online journal.)

Table 3
Hα Measurements (Rest-Frame) of the Low-Redshift QSOs

GALEX IAU ID	Hα Width (Å)	EW (Å)	Log Flux (10^{-17} erg cm^{-2} s^{-1} Å^{-1})
GALEX J075304.64+252436.6	47.3	102.3	−14.01
GALEX J154912.35+030641.8	109.0	43.9	−14.57
GALEX J140816.07+015528.5	57.2	51.7	−14.31
GALEX J024559.00−074500.0	86.1	127.3	−14.27
GALEX J092308.35+561455.9	114.1	53.7	−14.43
GALEX J024703.23−071421.5	73.3	70.8	−14.06
GALEX J161350.62+494155.8	79.0	101.5	−14.35
GALEX J153219.90+033811.1	94.1	61.4	−14.46
GALEX J235554.21+143653.3	53.4	335.7	−13.34
GALEX J091729.54+603143.7	79.0	213.7	−13.55
GALEX J141934.24+033153.3	86.0	188.7	−13.68
GALEX J091635.57+602722.4	98.8	239.6	−13.71
GALEX J223232.89−093633.9	95.7	90.7	−14.46
GALEX J211204.86−063534.7	80.0	297.0	−13.14
GALEX J233254.40+151305.6	145.7	127.6	−13.45
GALEX J020946.30−083349.6	90.4	147.6	−13.91
GALEX J223553.88+142805.7	96.3	282.3	−13.72
GALEX J223336.68−074336.1	143.8	102.3	−13.96
GALEX J101434.17+001708.4	76.8	59.9	−14.46
GALEX J224936.64+132038.3	107.9	156.3	−14.06

(This table is available in its entirety in machine-readable and Virtual Observatory (VO) forms in the online journal. A portion is shown here for guidance regarding its form and content.)

absolute luminosity. The spectral slope was measured as the ratio of fluxes integrated in two intervals which are rather free of conspicuous features in most spectra: rest wavelengths 3500–3700 Å and 6000–6400 Å. We compared several quantities, and we show six interesting cases in Figure 10. No obvious correlation is seen with the FUV–NUV color. The Hα flux, and EW, increase with absolute UV luminosity, and to a much lesser extent with *u*-band luminosity, but not with luminosity at longer wavelengths. Similarly, the optical spectral slope possibly correlates with Hα EW and with UV luminosity (but not with optical luminosity: the *r* band is also shown in Figure 10): it becomes bluer for brighter UV luminosities, suggesting that for low QSO luminosity the galaxy relative contribution is more significant. There is a clear difference between pointlike and extended sources: the latter have a flatter (redder) optical slope and lower Hα emission, reflecting the contribution of the host galaxy. This result emphasizes the role of UV studies in extending the known properties of QSOs. If we restrict the sample around redshift $z = 0.2$, where we have a wider FUV–NUV-observed range and Lyα is at the peak of the filter's transmission, the scatter is much reduced in the correlations with absolute FUV luminosity, and some possible correlations with UV color emerge, but the number of points is then too scarce for robust conclusions. Alternative explanations for the blue FUV–NUV color may include a dust effect, depressing the NUV flux. However, it is not obvious that any known interstellar extinction law would have this effect at these redshifts: the 2175 Å dip, for instance, would lie at the upper (long wavelength) end of the NUV passband for redshift beyond 0.2, and the FUV would be more absorbed. There is no correlation of the Hα intensity with foreground $E(B - V)$.

Figure 11 shows the magnitudes of the low-redshift sample, and their median values connected by lines. The average SED of UV-normal QSOs in this redshift range is also shown for comparison. The extended sources differ from the pointlike ones. Among pointlike sources, the overall brightness of UV-normal QSOs is slightly lower than the UV-blue QSOs. The extended UV-blue and UV-normal samples have similar SED in the optical bands, showing similarity of the host galaxy which contributes to the flux. We performed this comparison both using dereddened magnitudes, where each photometric measurement was dereddened using $E(B - V)$ (Table 1) estimated from the Schlegel et al. (1998) maps, before averaging the sample, as well as using observed magnitudes without extinction corrections. The individual sources and the average SEDs shift correspondingly, by up to ∼0.4 mag in UV, but the relative differences among average SEDs remain the same.

While there is no UV spectroscopy for our objects, we examined UV *HST*–STIS archival spectra of a sample of QSOs published by Shang et al. (2005). None of them are included in the current *GALEX* MIS coverage, but a few are in the *GALEX* AIS (which has about 10 times shorter exposures than MIS data and therefore larger photometric errors). We also computed synthetic colors for the Shang et al. sample convolving the observed *HST*/STIS spectral fluxes with the *GALEX* transmission bands. We show their position on the color–color diagram (Figure 1, small teal diamonds). A few of the Shang et al. (2005) QSOs have FUV–NUV only slightly bluer than 0.1, while the rest have typical FUV–NUV colors. The QSOs in the STIS sample with FUV–NUV <0.1 have optical spectral slope and Hα emission similar to the standard QSO template, but most display stronger Lyα and C IV, and a range of UV slopes (steeper, similar, but also flatter, than the average). The comparison, although limited to a different sample than ours and to a few bright objects, suggests that unusual UV properties may exist that cannot be predicted from the optical data.

4.2. The High-Redshift QSOs

The photometric SEDs of the 21 UV-blue QSOs with redshift between 1.7 and 2.6 are shown in Figure 12, and their optical spectra in Figures 13 and 14. The QSO with the highest redshift in the sample ($z = 2.6$) has an extremely red optical spectrum and appears as a very red faint object in the optical imaging (Figure 4). It also has much larger photometric errors than the rest of the sample: FUV = 22.41 ± 0.19, NUV = 22.67 ± 0.29, $u = 22.22 \pm 0.8$, $g = 21.40 \pm 0.23$, $r = 20.86 \pm 0.14$. The typical QSO FUV–NUV color for its redshift is significantly redder (more than 0.5 mag, Figure 1) so the object may still deserve attention.

At redshift $z = 2$, the NUV band includes flux in the rest-frame range 590–940 Å (the filter's $\lambda_{\rm eff}$ becomes rest-frame 757 Å) and the FUV band includes rest-frame 450–590 Å ($\lambda_{\rm eff} \sim$ rest-frame 500 Å). We speculate that a combination of steep flux rise toward rest-frame extreme-ultraviolet (EUV) and absorption below the Lyman limit may explain the observed FUV–NUV color. We constructed spectral templates with FUV flux rising more steeply than in standard templates, using two power-law slopes $F_\lambda \sim \lambda^\alpha$ with $\alpha = -0.6$ and -1.2. The average slope between 500–1200 Å in the large sample of Telfer et al. (2002) is $F_\nu \sim \nu^{-1.76}$, i.e., $\alpha = -0.24$ in F_λ. Our EUV-steep templates are shown with dark green diamonds in Figures 1 and 2. While they have synthetic FUV–NUV color bluer than the canonical template at redshift ∼2, they are still more than half-magnitude redder than the colors observed in our UV-blue sample. The fact suggests that a combination of both EUV flux rise at shorter wavelengths and a deep absorption below the Lyman limit may be required to explain the observed colors of

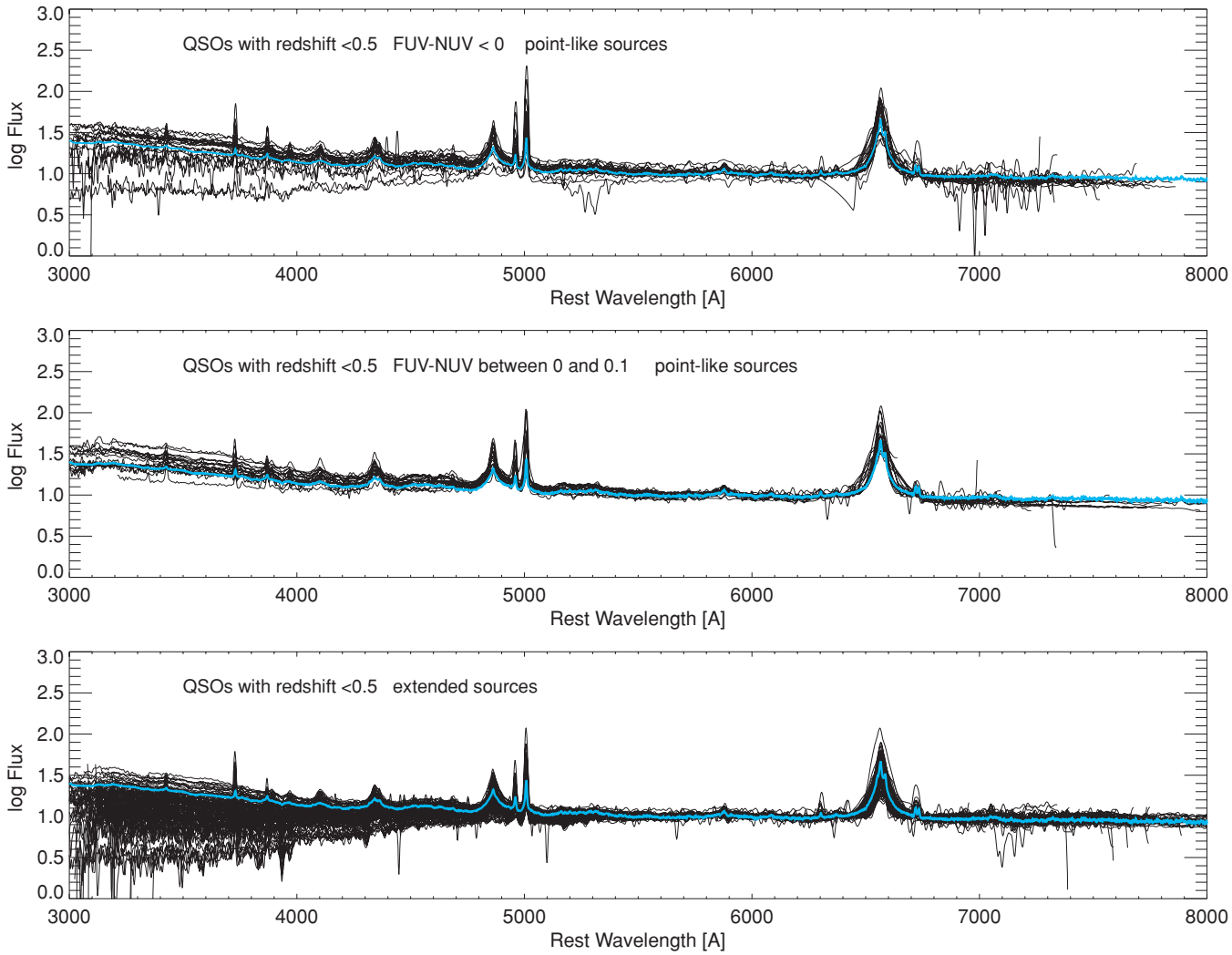

Figure 7. Visible spectra of the low-redshift QSOs. The fluxes (F_λ) have been scaled to a common value in the range 6000–6500 Å. Because of the large number of objects, we plot the pointlike sources in two groups, separated by FUV–NUV color. While the general spectral features are well represented by the template (cyan), stronger emission lines (especially Hα) and spectral slopes bluer than the template are observed in most cases (note the log scale). The extended objects are plotted in the bottom panel. Most have a redder slope than the template, and there is a mix of broad and narrow lines.

our UV-blue QSOs. The suggestion is supported by Figure 6, showing the absolute NUV luminosity of our UV-blue sample to be lower than average. This can also be appreciated in Figure 12 which shows all the observed magnitudes for our high-redshift sample. The Lyman limit in this redshift range lies between the NUV and u bands, and the Lyman drop is clearly seen. The line shows the median values, and only the object with a red optical spectrum mentioned above differs significantly (shown by the dotted line). Figure 12 also shows the median magnitudes for UV-normal QSOs from the MIS survey, with the same redshift range and error cuts. The average FUV–NUV is much "redder" for the UV-normal QSOs, consistent with our selection. The UV-blue QSOs are fainter in the NUV band, which is sampling the Lyman limit at these redshifts. Thus, our QSOs sample may have somewhat more extinction and more severe absorption below the Lyman limit. Three of the UV-blue QSOs have strong BAL-type C IV absorption (Figure 13). Their Lyman discontinuities (estimated from the broadband photometry, as defined in Figure 15) are very large for two of them and smaller than average for one. Thus, it is not clear whether BAL absorbers contribute significantly to the Lyman drop.

Binette & Krongold (2008, and references therein) discuss the spectrum of Ton 34, an unusual QSO with an enhanced "Lyman valley" in its UV spectra (*International Ultraviolet Explorer* (*IUE*) and *HST*), which can be reproduced by their models of absorption from carbon crystalline dust (nanodiamonds). Ton 34 is at redshift $z = 1.93$ and we investigated whether it could be a possible counterpart of our UV-blue QSOs. It is not included in the *GALEX* surveys to date (it is just outside the edge of an observed *GALEX* field), so we estimated *GALEX* FUV and NUV magnitudes by convolving the *IUE* SW and LW spectra of Ton 34 with the *GALEX* filters, and obtained FUV–NUV ∼1.3, close to the expected color of the UV-normal sample at this redshift and much redder than our UV-blue QSOs. This color estimate is uncertain because in the *IUE* spectra the signal is close to the background limit, and *HST* spectra of Ton 34 do not even cover one of the *GALEX* bands. The *GALEX* FUV band includes flux longward of 1344 Å, while in the *IUE* spectrum of Ton 34 the flux is very steeply rising just shortward of this limit. Therefore, a slightly more redshifted analog of Ton 34 would produce a much brighter FUV magnitude.

Models of crystalline dust absorption by Binette & Krongold (2008) show that the general effect is a very deep Lyman valley,

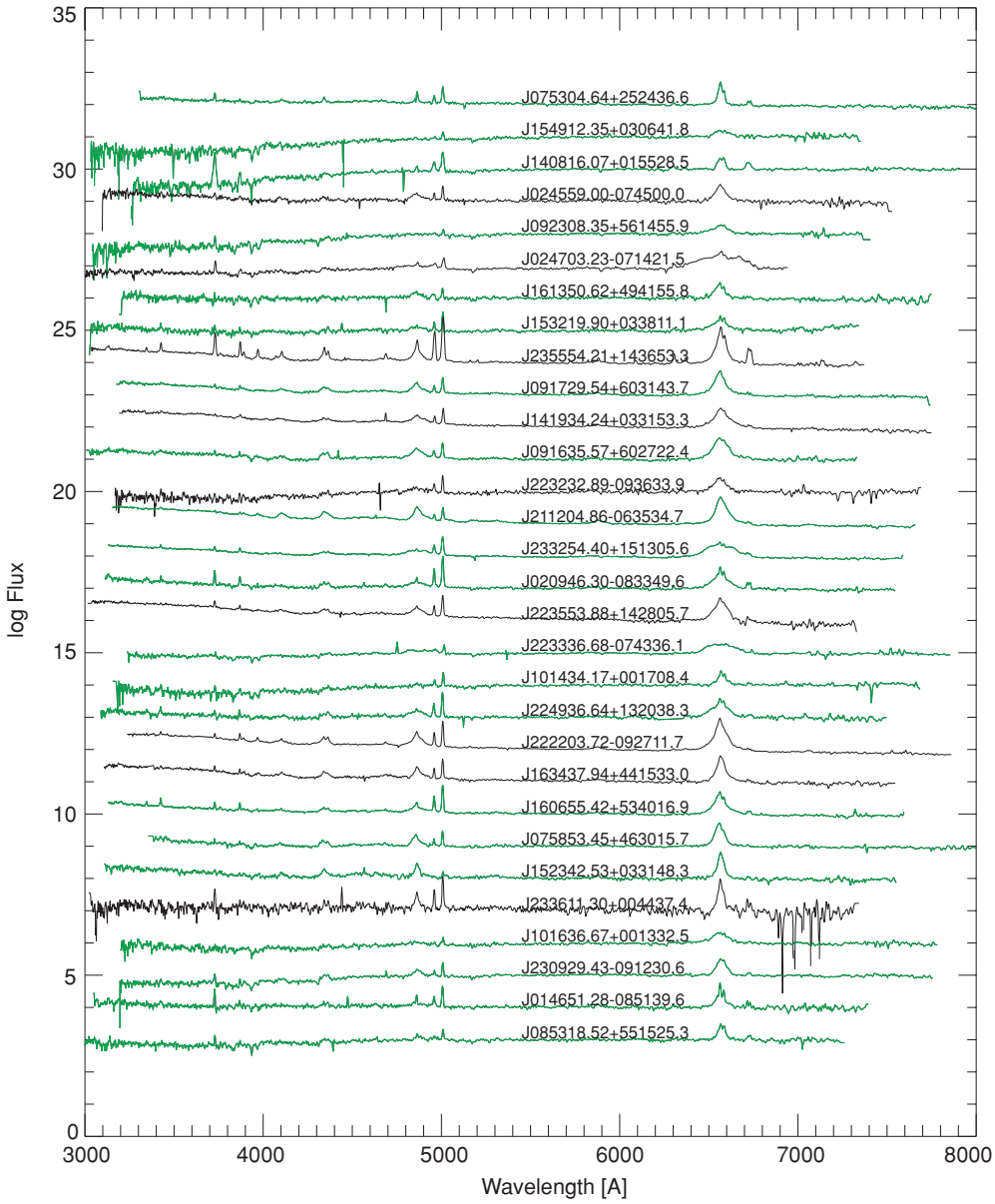

Figure 8. Sample spectra of low-redshift UV-blue QSOs, labeled by the *GALEX* IAU identifier. Fluxes are scaled to have a constant offset at 6000–6500 Å. Spectra of extended objects are plotted in green/gray, and of pointlike sources in black. The order is FUV–NUV bluer to redder, top to bottom, but the spectral features, especially the slope, do not show any obvious trend with UV color.

(A color version of this figure is available in the online journal.)

and in more detail the relative amounts of absorption in the wavelength ranges sampled by the *GALEX* FUV and NUV filters at $z \approx 2$ vary according to the dust geometry and composition. For example, comparison of dust models in figure A.2 of Binette & Krongold (2008) suggests that a lower column density of the carbon crystalline dust screen (or an intrinsic SED steeper toward short wavelengths) may produce a higher FUV flux, and small grain dust (similar composition as MW dust, i.e., silicate and graphite grains, but grain sizes much smaller than MW dust and larger than nanodiamonds) would cause a significant depression of the observed-NUV flux but less reduction of the observed FUV at the redshift of our high-z UV-blue QSOs. This effect would be qualitatively consistent with the SED of our UV-blue QSOs. From broadband photometry alone, it is not possible to separate effects of dust absorption and intrinsic SED slope, therefore we can only speculate that the observed FUV–NUV colors in our sample are qualitatively compatible with absorption from dust with grains differing from the MW dust (smaller grains), and possibly a steeper flux rise toward EUV. The question remains open as to what causes the extremely blue FUV–NUV colors, and whether these objects have known counterparts with similar properties, until UV spectroscopy can be obtained.

We have measured the emission lines of C IV and C III (EW, total flux, and full width (FW) at 10% of the peak flux above the local continuum) from the SDSS spectra. Typical errors are of the order of 10%. Lyα is generally too near the end of the optical spectra and could be measured only in 10 cases. The C III line is free of absorptions but some QSOs have significant BAL and interstellar absorptions in the C IV line. The emission line properties do not correlate at all with the FUV–NUV color. The FUV–NUV color does correlate with the $g-i$ color, which may indicate that extinction is involved, and with redshift, although weakly, in the sense that higher redshift objects are more

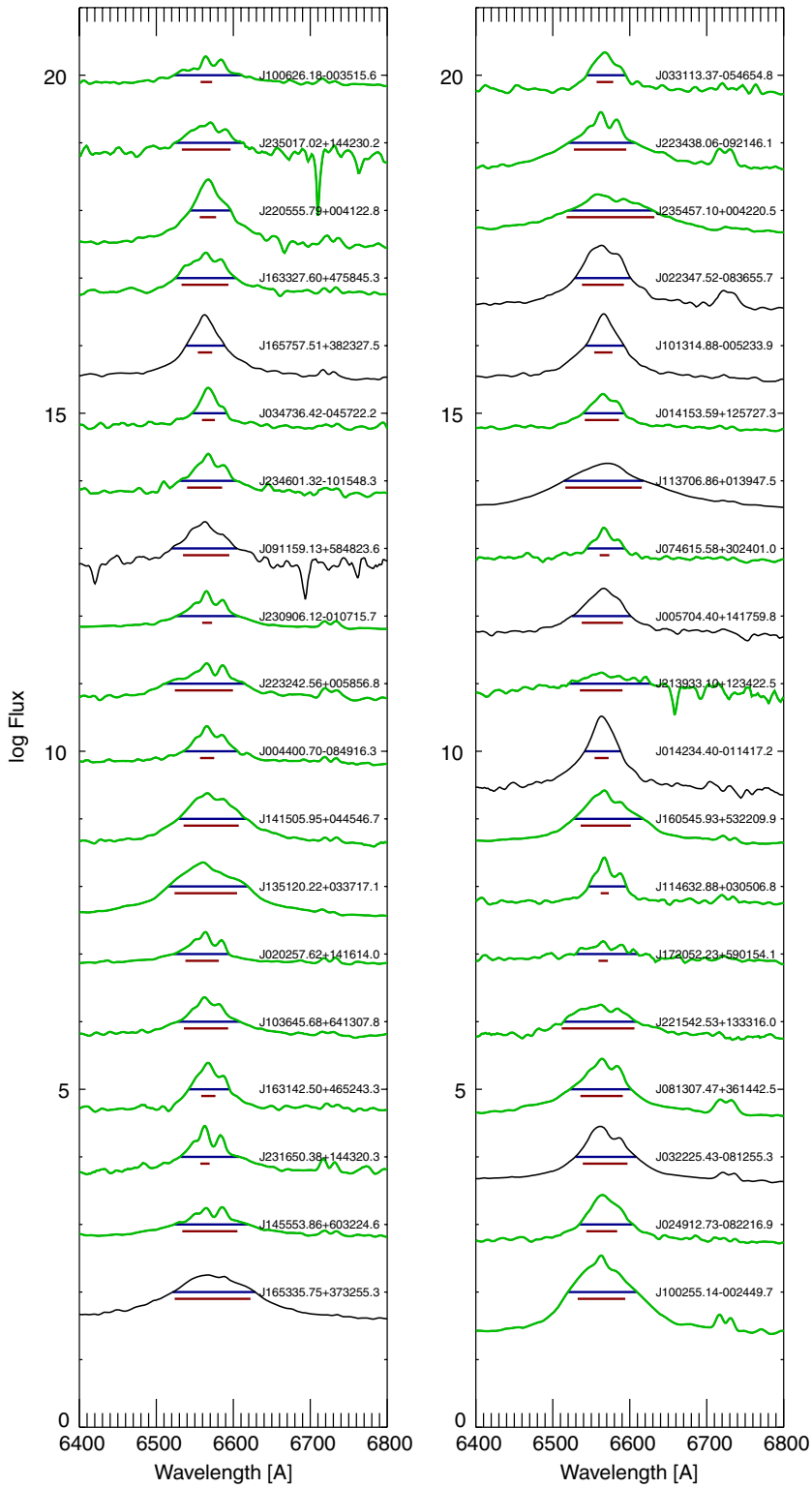

Figure 9. Hα line of about one-third of the low-z objects (black: pointlike; green: extended sources). Profiles vary from very broad to narrow, to broad profiles with superimposed narrow components. The line width measured with our code (see the text) is shown with a blue horizontal line, the width from the SDSS pipeline with a red line (plotted lower for clarity). Fluxes (F_λ) are offset for clarity.

UV-blue (Figures 5 and 15). This is what we would expect in the rest wavelengths below the Lyman limit, where the continuum is rising again. The Lyman discontinuity is larger for higher redshifts too, which is likely caused by where it lies between the NUV and u bandpasses. The emission line EW is larger for fainter FUV magnitudes, but scales more slowly than the continuum flux. The line FW is higher for more luminous QSOs, based on their g-band magnitudes (rest-frame FUV). Flux and EW of C III and C IV lines correlate with the Lyman discontinuity, but not the line FW. Thus, there is a connection between line emission and the EUV continuum. Figure 15 shows some of these correlations; the Spearman's ρ significance test

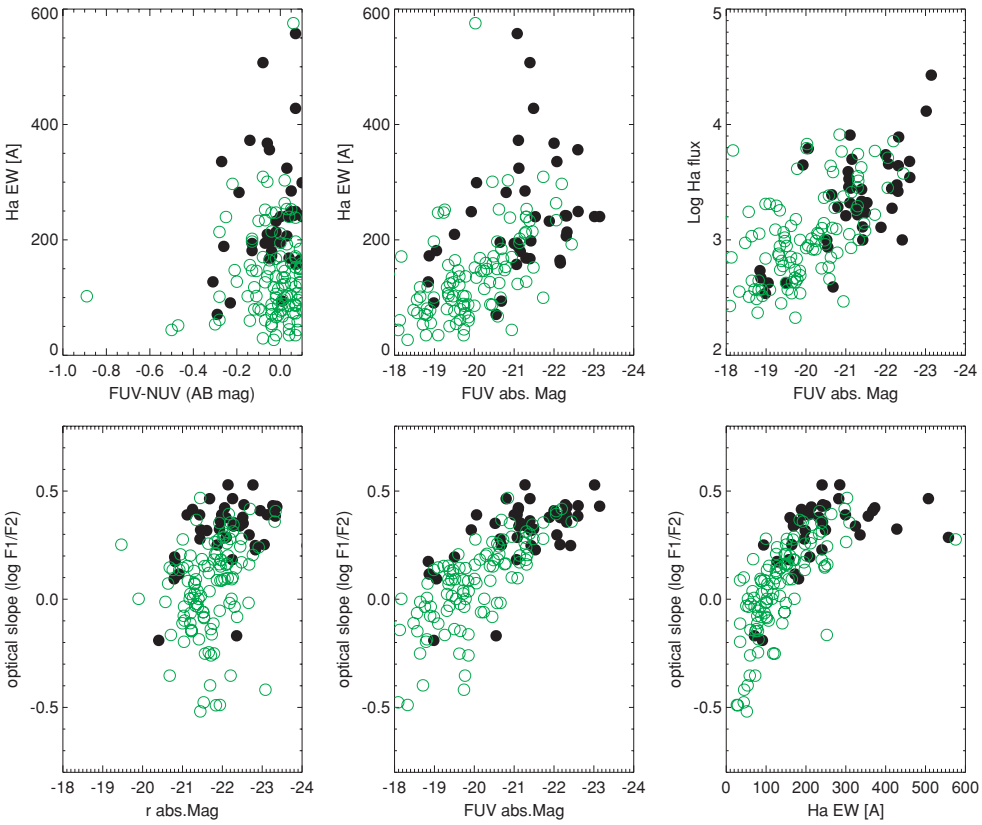

Figure 10. Hα emission and optical spectral slope $F_\lambda 1$(3500–3700 Å)/$F_\lambda 2$(6000–6400 Å) of the low-redshift QSOs show correlation with the UV absolute magnitude, but not with the FUV–NUV color or optical absolute magnitude. Spectral slope, and to a lesser extent the Hα flux and EW, differ between pointlike (black dots) and extended (green/gray circles) samples. The Hα flux is in units of 10^{-17} erg cm^{-2} s^{-1}. If we restrict the sample to redshift $z = 0.15$–0.25 (where Lyα is centered in the FUV filter) the correlations in the right and middle panels become tighter.

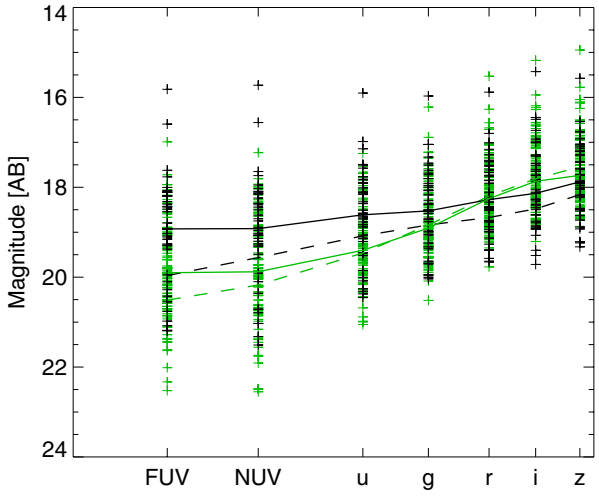

Figure 11. *GALEX* and SDSS magnitudes for the low-redshift sample, and median magnitudes as solid lines (black: pointlike; green: extended sources). Magnitudes are plotted at the $\lambda_{\rm eff}$ of each filter, on a logarithmic wavelength scale. Dashed lines are the median for the comparison sample of UV-normal QSOs. Lyα lies within the FUV channel for these objects and will contribute to the FUV–NUV color. In FUV–NUV the greatest difference is seen, consistent with our sample selection. For both UV-blue and UV-normal samples, we simply averaged all QSOs within the same redshift range. The number of objects across the redshift range however is distributed nonuniformly for each sample; if we eliminate the weight of the relative number of objects and combine median values in small redshift bins, the curves change very little, and the general trend is the same. Because average magnitudes vary with redshift, average properties of samples vary according to how the sample is defined. Therefore, small differences should not be overinterpreted but we believe that the general trend is robust.

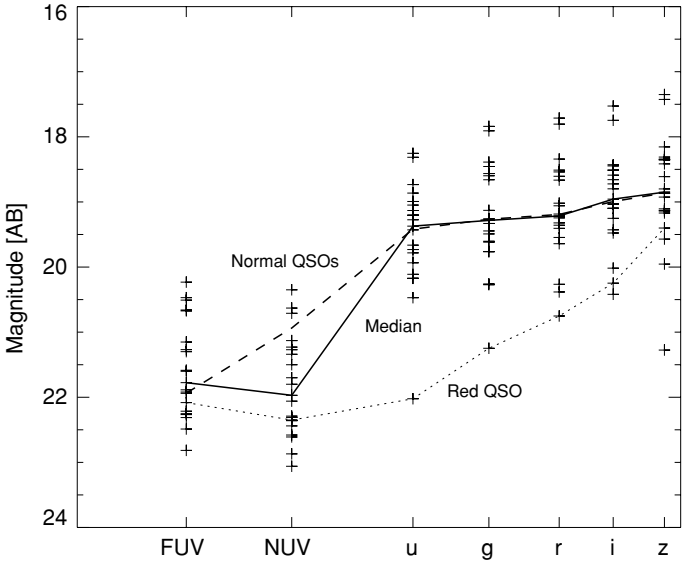

Figure 12. *GALEX* and SDSS average magnitudes for the high-redshift sample. The Lyman limit lies between the NUV and u bands in this redshift range. The line is the median values for each and the dotted line is the one discrepant QSO with a very red optical spectrum. The dashed line is the average from a sample of UV-normal QSOs within the same redshift range (1.7–2.4). Photometry of each object has been corrected for interstellar extinction using $E(B-V)$ given in Table 1; the same correction was applied to the UV-normal sample before deriving the average. A plot without extinction correction applied is qualitatively very similar, shifted slightly toward fainter values, especially in UV, but the relative differences remain the same. Magnitudes are plotted at the $\lambda_{\rm eff}$ of each filter, on a logarithmic wavelength scale.

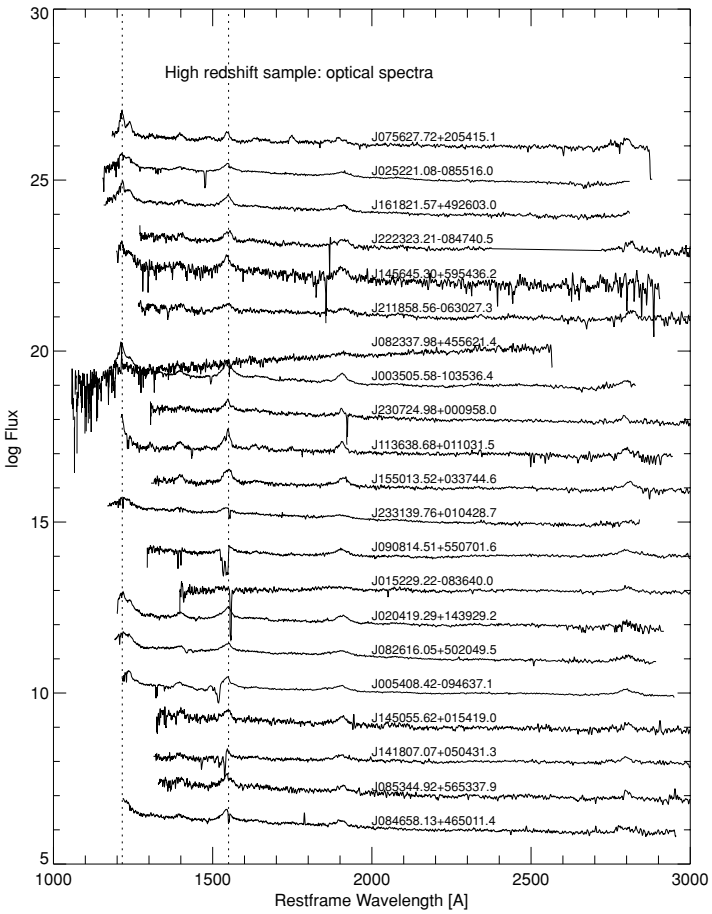

Figure 13. Optical spectra of the high-z sample, plotted in the rest-frame wavelength. The spectra (in F_λ) are scaled so to have a constant offset at 2000–2500 Å. They are ordered (top to bottom) by FUV–NUV (bluer to redder), and labeled with their *GALEX* IAU identifier. Only for a few objects Lyα is included in the spectrum, at the edge of the observed range.

gives a probability of correlation (clockwise from top left) of 99%, 94%, 58%, and 99%.

While the dust absorption affects more the continuum, the ionization would be reflected by the line ratios. Binette & Krongold (2008, and references therein) discuss also the effects of shock ionization versus photoionization. It is interesting that their models show low C IV and N V relative to Lyα, compared with UV-normal QSOs. We measured Lyα+N V and C IV in our high-redshift UV QSOs where possible (10 cases). The line flux ratios may be useful diagnostic since shocks may not be related to the continuum. Therefore, we also examined SDSS spectra of UV-normal QSOs in the same redshift range and compared their line strength with the UV-blue sample. We extracted spectroscopically confirmed QSOs in the same redshift range $z = 1.7$–2.5, but with FUV–NUV > 0.1, from our master catalog of matched sources. We found 420 objects, compared with our 21 with FUV–NUV < 0.1. We imposed the same error cuts in FUV, which unfavors the red (normal) QSOs, so the ratio (5%) is a lower limit for the fraction of UV-blue QSOs compared with normal ones. The relative numbers however may be highly biased because the SDSS spectral targets were chosen with criteria not related to our UV selection. We measured the same line ratio only for the UV-normal comparison objects with $z = 2.2$–2.5, where Lyα is included in the optical spectra. The measurements are shown in Figure 16, where a linear fit is also shown; the formal probability of correlation is over 99%. The average line ratios for the UV-blue and UV-normal samples are given in Table 4. The average is 5.2 for our UV-blue sample and 3.7 for our normal comparison sample. The collisional model predicts a ratio of ~6.7, and the photoionization model 1.8. In one of our UV QSOs the ratio Lyα+N V/C IV is about 10, while Ton 34 has a ratio of 8.7. This bears out the similarity with Ton 34, and a dominance of collisional ionization, compared with UV-normal QSOs.

5. CONCLUSIONS AND SUMMARY

We analyzed 171 spectroscopically confirmed QSOs with FUV–NUV color bluer than 0.1, extracted from the *GALEX* MIS survey with complementary SDSS optical data. Most of these objects have redshift <0.5, and we speculate that Lyα emission enhanced up to a factor of 3 with respect to average templates, may explain the observed colors. Their optical properties are similar to those of UV-normal QSOs. Both photometric and emission line properties differ between pointlike and extended sources, reflecting the contribution from the host galaxy in the latter. The slope of their optical spectra and the strength of Hα (flux and EW) correlate (increase) with intrinsic UV luminosity. Lyα goes through the *GALEX* FUV band in the redshift range of these objects, between 0.1 and 0.5, therefore the resulting effect on the broadband FUV magnitude is a combination of the line intensity and the filter's transmission curve. A restricted subsample with redshift around 0.2 (where Lyα is at the peak of the filter's transmission) seems to show

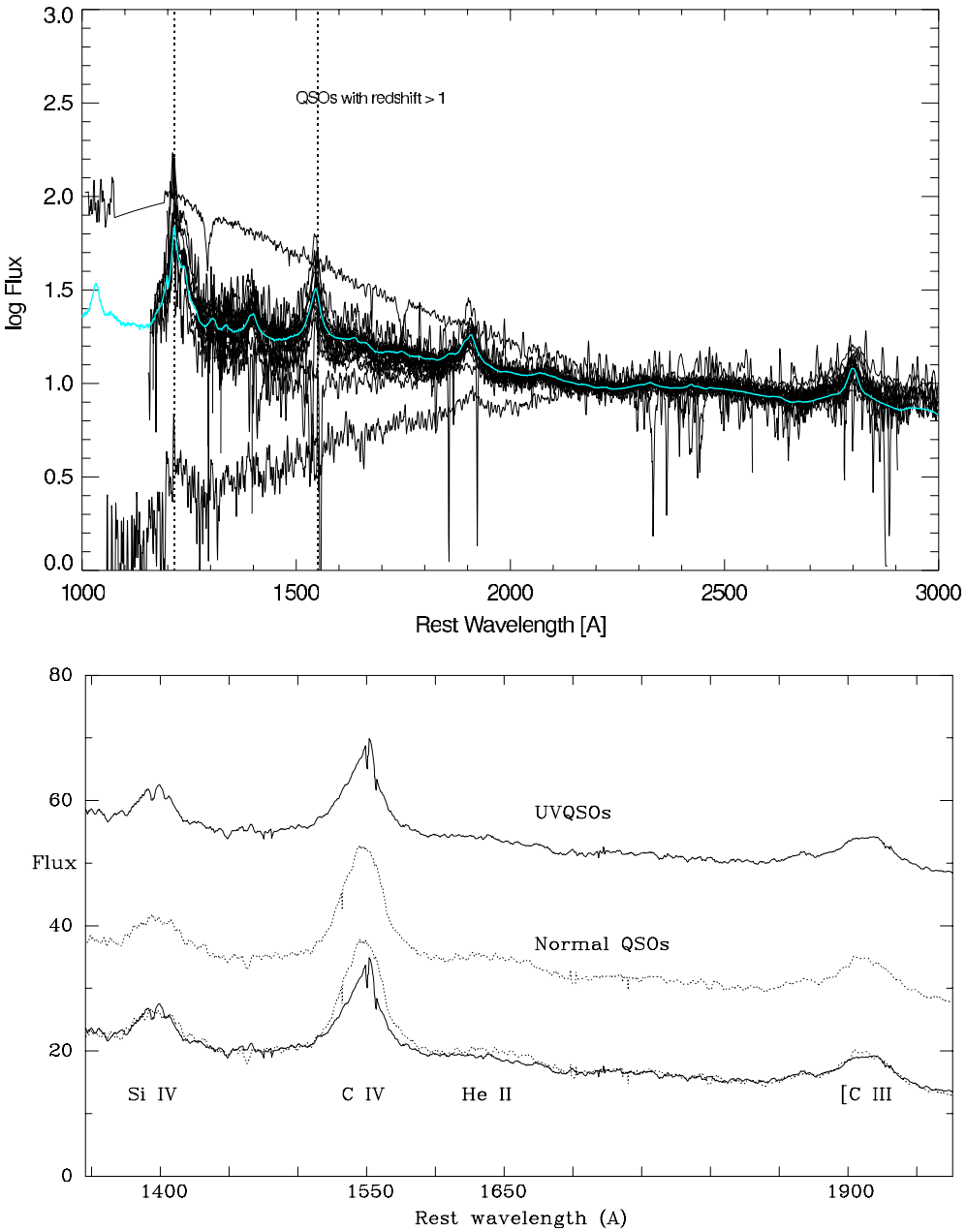

Figure 14. Visible spectra of the high-redshift QSOs. Top: fluxes (F_λ) have been scaled to a common value in the range 2000–2500 Å. The "hottest" spectrum is the hot star, misclassified by the SDSS pipeline as a QSO of redshift $z = 2.7$: in the observed wavelength scale, the absorptions are the Balmer lines. Vertical dotted lines mark Lyα and C IV λ1550 positions. The cyan spectrum is the standard QSO template. The extremely red spectrum is discussed separately (Figure 4). Bottom: averaged optical spectra of our UV-blue sample, and UV-normal comparison sample in the same redshift range. The C IV doublet is different. For Lyα no conspicuous difference is seen, but this line is available only for few "UV-blue" QSOs, making the comparison not significant.

tighter correlations but it is statistically insufficient to support conclusions. The UV luminosity is brighter (∼0.5–1 mag on average) than that of our UV-normal comparison sample, the difference being larger in FUV and for the pointlike objects (Figures 6 and 11).

Our sample of UV-blue QSOs also includes 21 objects with redshift between 1.7 and 2.6. Their photometric errors are generally large, the combined FUV–NUV 1σ errors are between 0.1 and 0.37 mag, but our FUV–NUV selection limit (FUV–NUV <0.1) is bluer than typical QSO colors at this redshift by more than 0.5 mag, and the observed FUV–NUV colors are bluer than the typical color by up to 1 mag or more (Figure 1). For these UV-blue QSOs at higher redshift, we speculate that a combination of unusually strong absorption in *GALEX*-NUV (rest-frame ∼600–900 Å) and EUV-steeply rising flux (*GALEX* FUV ∼ rest-frame 450–590 Å) may explain the FUV–NUV color. This is suggested by two facts. First, ad hoc templates with flux rising toward rest-frame EUV more steeply than in canonical templates, produce observed FUV–NUV colors bluer than the average template (Figure 2), but still redder than our selection limit by 0.2 mag and redder than most of our UV-blue sample by up to 1 mag. Second, comparison with average SED of a UV-normal QSO sample, shows the NUV luminosity of the UV-blue sample to be fainter, suggesting absorption in the observed NUV. Dust with composition similar to the typical MW dust but smaller grains and carbon crystalline nanosized grains

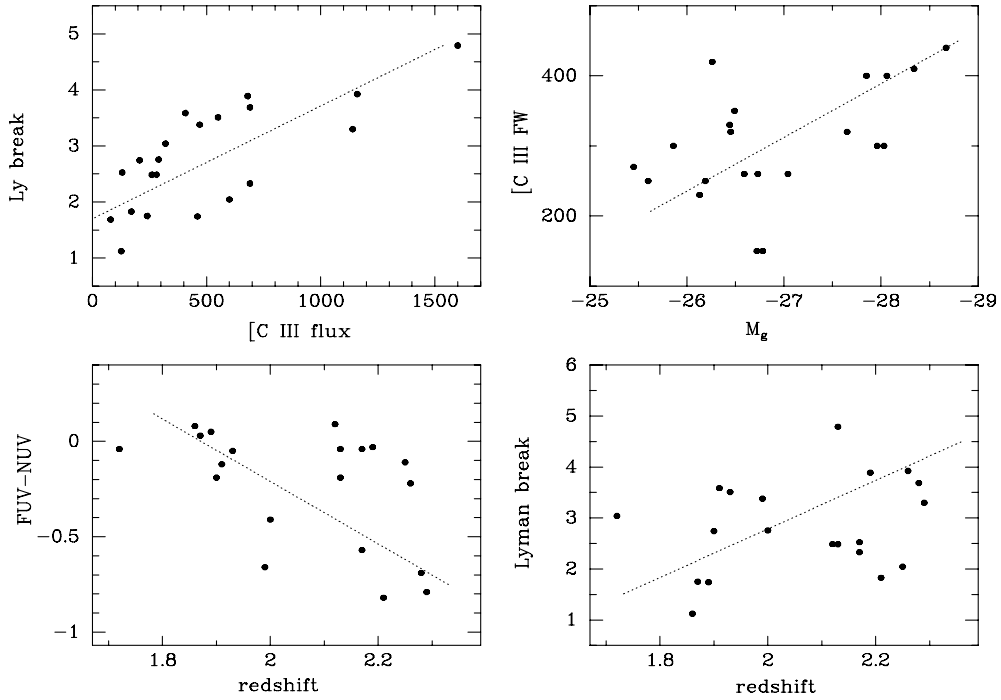

Figure 15. Quantities which show trends with UV data in the high-redshift sample. The Lyman break value is the mean of the two *GALEX* magnitudes minus the mean of the five SDSS magnitudes. The dotted lines are linear fits to the points. The red QSO (see Figure 4) is very discrepant in the lower two plots and is off-scale and not fitted by the line. FUV–NUV is in AB magnitudes. The FW (in Å) plotted in the upper-right panel is measured at 10% of the peak flux above the local continuum, by line profile fitting.

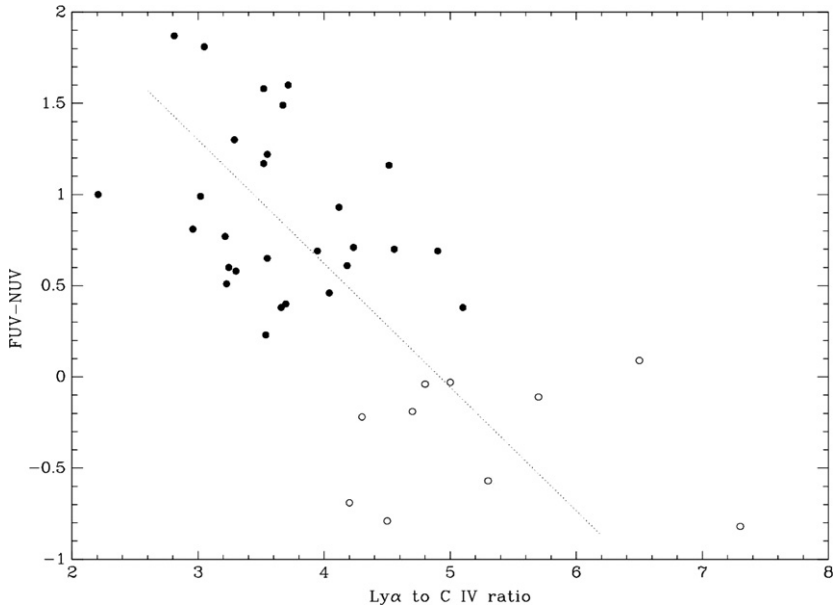

Figure 16. Ratio of Lyα+N v to C iv emission for the UV sample (circles) and a comparison sample with similar redshift but FUV–NUV >0.1 (filled dots). Although the sample is very limited, the UV-blue QSOs tend to have a higher ratio, suggestive that collisions may be more relevant. The line is a linear fit.

(nanodiamonds) would cause absorption in the observed NUV band, according to the models of Binette & Krongold (2008), which may qualitatively account for the observed FUV–NUV colors. UV spectroscopy is needed to pinpoint the cause for the FUV–NUV color of these objects. The Lyα to C iv ratio is stronger in the optical spectra of the UV-blue QSOs than in the UV-normal comparison sample (at the >95% confidence level from the Kolmogorov–Smirnov test, although both samples are very small, see Figure 16), suggesting collisional ionization to be more relevant in the UV-blue QSOs.

The group of UV QSOs at $z \sim 2$ may probe a particularly relevant phase of galaxy formation, tightly connected with the formation of the massive central black hole. In current QSO/Spheroid co-evolution models (e.g., Granato et al. 2004), the power of the central QSO rises almost exponentially and quickly stops the star formation process. During the previous phase it is strongly dust enshrouded and not visible except in X rays. A phase of decreasing (but still significant) extinction follows, and finally a shining phase until the fuel is consumed. A quick transition is expected between dust extinguished and

Table 4
Average Line Measurements of the High-Redshift Sample

	UV QSOs	UV-Normal QSOs
No. of objects	10	28
Lyα/C IV	5.23	3.68
Lyα flux	440	285 (365)
C IV flux	90	75 (96)
C III flux	52	41 (52)
C IV/C III	1.74	1.82

Notes. Values in parentheses for UV-normal QSOs are continuum corrected. Note that the average of the ratios and the ratio of the averages are not the same because the average fluxes weigh the high values more. Theoretical values for Lyα/C IV ratio are 6.7 for collisional ionization and 1.8 for photoionization.

not extinguished phases for QSOs at high z. The relative percentage of UV-blue QSOs could be a measure of the relative lifetimes of that phase. As explained in Section 4.2, within our sample of matched *GALEX*–SDSS sources, the number of spectroscopically confirmed QSOs with FUV–NUV <0.1 is about 5% of those with redder FUV–NUV in the redshift range around 2. However, this number may be highly biased because the availability of SDSS spectra is serendipitous from the point of view of our selection. The fraction of sources with available spectra is not uniform across the range of optical and UV colors, and redshift, of our photometric candidate sample. Spectroscopic selection especially favors the brightest samples, while Bianchi et al. (2007, 2008) show for example a steep increase of UV-blue extragalactic object candidates at faint magnitudes. Some UV-to-optical color ranges are also contaminated by stellar objects and the purity of photometric candidate samples varies greatly according to the colors regime and parameters. The aim of this work was to point out that a non-negligible sample of UV-blue QSOs exist, and explore their nature. Statistical considerations will be addressed using a larger sample.

Another possible bias may arise from variability, which is frequently observed in QSOs. Serendipitous repeated UV observations for our sample show variations by $>3\sigma$ in some objects, and in many cases the FUV–NUV in repeated measurements is redder than in our selected data set, making some of these objects UV-normal or close to normal in some of the measurements, and extremely blue in others. We have tried to exclude as thoroughly as possible imaging or pipeline artifacts, using the flags provided by the pipeline and identifying several additional unreliable measurements by individual analysis. However, we should keep in mind that pipeline photometry of large data sets has statistical value, and in particular the combination of *GALEX* and SDSS source catalogs over a large area of the sky proved invaluable to characterize elusive classes of objects (Bianchi et al. 2007), but it should not be overinterpreted for individual objects.

For both the low-redshift QSOs where Lyα may be stronger (possibly up to three times) than in typical QSO templates, and the high-redshift QSOs where deep Lyman valley absorption may occur, UV spectroscopy is needed for a conclusive explanation of the FUV–NUV color, and to assess whether these are similar to some known objects. Our analysis showed that the *GALEX* photometry provides a unique sieve to select these UV-blue QSOs, whose optical properties are not unusual. The analysis of this limited spectroscopic sample, and its average photometric properties, also provides useful information to separate these QSOs from stellar binaries with a hot WD in our larger samples of photometric candidates (e.g., Bianchi et al. 2007, 2008), as shown in Figures 1 and 2. The contamination of these objects in stellar samples may be very significant at faint magnitudes, because the density of MW hot WDs, extracted from *GALEX* catalogs, at MIS depth (UV mag ~ 22.7 AB mag) is much lower than that of QSOs (Bianchi et al. 2007, 2008).

We are very grateful to Vahram Chavushyan, Lucio Buson, and Sebastien Heinis for discussions at different stages of this work, and to the anonymous referee for many comments which led to useful clarifications and improved the paper. More information and related papers are available at the author's Web site at http://dolomiti.pha.jhu.edu. *GALEX* is a NASA Small Explorer, launched in 2003 April. We gratefully acknowledge NASA's support for construction, operation, and science analysis of the *GALEX* mission, developed in cooperation with the Centre National d'Etudes Spatiales of France and the Korean Ministry of Science and Technology. The data presented in this paper were obtained from the Multimission Archive at the Space Telescope Science Institute (MAST). STScI is operated by the Association of Universities for Research in Astronomy, Inc., under NASA contract NAS5-26555. Support for MAST for non-*HST* data is provided by the NASA Office of Space Science via grant NAG5-7584 and by other grants and contracts.

Facilities: GALEX, *Sloan*, *HST* (*STIS*)

REFERENCES

Bianchi, L. 2008, Ap&SS, http://www.springerlink.com/content/h3583v2919162223/
Bianchi, L., et al. 2005, ApJ, 619, L27
Bianchi, L., et al. 2006, in UV Astronomy: Stars from Birth to Death, ed. A. I. Gomez de Castro & M. Barstow (Madrid: UCM Editorial Complutense), 95
Bianchi, L., et al. 2007, ApJS, 173, 659
Bianchi, L., et al. 2008, in Future Directions in Ultraviolet Spectroscopy, ed. Van Steenberg et al., in press
Binette, L., & Krongold, Y. 2008, A&A, 478, 739
Granato, G. L., De Zotti, G., Silva, L., Bressan, A., & Danese, L. 2004, ApJ, 600, 580
Hutchings, J. B., & Bianchi, L. 2008, PASP, 120, 275
Hutchings, J. B., Scholz, P., & Bianchi, L. 2009, AJ, 137, 3533
Martin, C., et al. 2005, ApJ, 619, L1
Morrissey, P., et al. 2007, ApJS, 173, 682
Schlegel, D. J., Finkbeiner, D. P., & Davis, M. 1998, ApJ, 500, 525
Shang, Z., et al. 2005, ApJ, 619, 41
Telfer, R., et al. 2002, ApJ, 565, 773